Nanoscale

PAPER

View Article Online
View Journal | View Issue

Cite this: *Nanoscale*, 2025, **17**, 17312

Self-reconstruction of FeCoNiMoW high entropy alloy to boost OER activity with robust stability for anion exchange membrane water electrolyzer†

Lili Guo,‡[a] Yanan Huang,‡[b] Yue Qin,[a] Bin Chen,[c] Chang Liu,[a] Hao Chen,[b] Junfeng Zhang,[c] Xiangwen Zhang[a,d] and Qingfa Wang *[a,d]

Anion exchange membrane water electrolysis (AEMWE) is a promising advanced strategy for large-scale green hydrogen production. Developing highly active, stable, and low-cost oxygen evolution reaction materials is still challenging. Herein, a core–shell FeCoNiMoW@FeCoNiOOH electrocatalyst was fabricated by *in situ* self-reconstruction of FeCoNiMoW high entropy alloy prepared *via* the fast carbothermal shock method. The surface Mo and W as sacrificing agents were etched in the reconstruction of the catalyst to generate more oxygen vacancies and form the FeCoNiOOH-rich medium entropy alloy shell, which is enriched in more active species M-OOH (*i.e.*, NiOOH, CoOOH, FeOOH) to promote the OH adsorption. The medium/high entropy core–shell structure derived from self-reconstruction exhibited not only high activity but also excellent corrosion resistance, evidenced by an overpotential of 246 mV at 10 mA cm^{-2} and a robust stability of 1000 h at 100 mA cm^{-2}. Moreover, this core–shell FeCoNiMoW@FeCoNiOOH-based anion exchange membrane water electrolyzer demonstrated a low cell voltage of 1.74 V to achieve a practical current density of 1 A cm^{-2} and exhibited remarkable stability for 430 h with a decay rate of only 0.023 mV h^{-1}. This work provides guidance on designing cost-effective and outstanding corrosion-resistant OER electrocatalysts for anion exchange membrane water electrolysis.

Received 27th March 2025,
Accepted 3rd July 2025

DOI: 10.1039/d5nr01277e

rsc.li/nanoscale

1. Introduction

Fossil energy depletion and environmental pollution are two major problems in the world today.[1] Hydrogen energy, owing to its high energy density, environmental friendliness, and sustainability, is an ideal clean energy source and the most effective energy carrier for alleviating the pressure of energy deficiency.[2–4] Currently, hydrogen is mainly derived from coal, oil, and natural gas reforming, consuming a large amount of fossil energy, exacerbating the energy crisis and environmental pollution, and deviating from the goal of clean energy.[3] Electrolytic water splitting is considered to be the most promising hydrogen production technology, owing to its efficiency, environment-friendliness, and sustainability.[5,6] Anion exchange membrane water electrolysis for large-scale hydrogen production is considered an advanced strategy.[7] Water electrolysis is divided into two half-reactions: anodic oxygen evolution reaction (OER) and cathodic hydrogen evolution reaction (HER). The slow OER kinetics induce the high overpotential of the anodic OER, which impedes the improvement of overall electrolysis efficiency.[8] Therefore, developing highly active and robust electrocatalysts for alkaline OER is essential for realizing the large-scale application of AEMWE. Conventional binary or ternary alloys have poor OER catalyst activity due to fewer active sites, as well as their large mixed-phase gaps and poor corrosion resistance, which hinders their further application.[9–12] Fabricating multiple-component catalysts is a promising strategy for constructing excellent OER catalysts due to the synergistic interactions of components and the enhanced electrical conductivity. High-entropy alloy materials (HEAs) have recently aroused considerable interest in catalyzing water-splitting reactions because of the compositional flexibility, structural stability, and synergy between various elemental components. Therefore, HEAs have a natural advantage in the construction of multi-component catalysts and are expected to have high catalytic efficiency. The corrosion resistance of the catalysts can also be enhanced by adjusting the elemental composition.[13,14] The HEAs containing noble

[a]*Key Laboratory for Green Chemical Technology of the Ministry of Education, School of Chemical Engineering and Technology, Tianjin University, Tianjin 300072, China. E-mail: qfwang@tju.edu.cn; Fax: +86-22-27892340; Tel: +86-22-27892340*
[b]*State Key Laboratory for Chemo/Biosensing and Chemometrics, College of Chemistry and Chemical Engineering, Hunan University, Changsha 410082, China*
[c]*State Key Laboratory of Engines, School of Mechanical Engineering, Tianjin University, Tianjin 300072, P.R. China*
[d]*Collaborative Innovation Center of Chemical Science and Engineering (Tianjin), Tianjin University, Tianjin 300072, China*

†Electronic supplementary information (ESI) available. See DOI: https://doi.org/10.1039/d5nr01277e

‡These authors contributed equally to this work.

metals have been widely investigated for OER. Cai *et al.* prepared FeCoNiCuIr high entropy alloy nanoparticles with adjustable sizes in the range of 16–32 nm by a simple one-step heating method, which exhibited an overpotential of 360 mV at a current density of 10 mA cm^{-2}, a Tafel slope of 70.1 mV dec^{-1}, and a stability of 10 h.[15] Huang *et al.* synthesized a FeCoNiRu high entropy alloy catalyst using a hydrothermal method, and exhibited good OER performance with an overpotential of 243 mV@10 mA cm^{-2} in a 1 M KOH electrolyte but short durability of 40 h.[16] Wang *et al.* synthesized FeCoNiMnRuLa/CNT catalysts by carbothermal shock method, and the introduction of the rare earth element La breaks the lattice order of FeCoNiMnRu. The catalyst activity showed an overpotential of 281 mV for OER at a current density of 10 mA cm^{-2} for stable electrolysis of 200 h.[17] Wang *et al.* synthesized FeCoNiCuPd high-entropy alloy catalysts by magnetron sputtering, with an overpotential of 194 mV at a current density of 10 mA cm^{-2} and poor stability of 36 h at a high current density of 100 mA cm^{-2}.[18] These noble metal HEAs showed excellent activity, but the stability was still relatively poor, especially at high current densities. Besides, these high-entropy alloys still contain a high content of noble Ru and/or Ir metals, which limits their practical applications on a large scale. It is imperative to seek non-noble metal catalysts with excellent activity and high stability. Recently, extensive research has been conducted on alternative catalysts such as sulfide,[19] phosphides,[20] borides,[21,22] metal oxides,[23] and metal hydroxides.[24] However, both the activity and stability of these catalysts need further improvement. Sharma *et al.* synthesized Co–Fe–Ga–Ni–Zn high-entropy alloy catalysts. After cyclic voltammetry, the surface was converted into high entropy (oxygen) hydroxides (HEOs), which exhibited a 370 mV overpotential at a current density of 10 mA cm^{-2}, and a short durability for 10 h.[25] Zhang *et al.* synthesized a high-entropy alloy FeCoNiMoCe by adding the rare earth element Ce. This catalyst had an overpotential of only 260 mV at a current density of 10 mA cm^{-2} but poor stability (12 h).[26] Bian *et al.* prepared a high entropy alloy FeCoNiCuW catalyst by constant current electroplating, which exhibited an overpotential of 247.3 mV at 10 mA cm^{-2} in 1 M KOH electrolyte and short stability of 24 h.[27] Yi *et al.* prepared a HEA FeCoNiCrMo to prevent Ni/Co overoxidation by doping with high valence metals, which exhibited a good overpotential of 303 mV@100 mA cm^{-2} and good stability of 120 h@50 mA cm^{-2}.[28] Although these high-entropy alloys exhibited high activity, their stability was still less than satisfactory. To improve the stability of electrocatalysts, researchers have employed various strategies, including elemental doping,[17,25,26] strain engineering,[29] and structural regulation.[30] However, the stability (<150 h@100 mA cm^{-2}) was still far less than the requirements for application. In addition, the application of high entropy alloys in AEMWE has still rarely been investigated. Only Lu *et al.* have synthesized a FeCoNiCuMo/NM high entropy alloy and tested its OER performance in AEMWE using this alloy as the anode, FeCoNiCuMo/CP as the cathode, and a commercial Fumatech FAA-3-50 anion exchange membrane. At a temperature of 50 °C, this catalyst achieved a current density of 1.777 A cm^{-2} at a high cell voltage of 2 V and considerable durability (100 h) at 100 mA cm^{-2}.[31] Up to now, no noble metal-free electrocatalysts with outstanding activity and excellent stability at high current densities (*e.g.*, 100 mA cm^{-2}, 1 A cm^{-2}) for AEWME have been reported. Therefore, it is urgent to develop low-cost, highly active, and stable non-precious metal OER electrocatalysts.

Transition metals Fe, Co, Ni, Mn, and Cu are promising active elements for OER, and the addition of high-valent transition metal elements (*e.g.*, Cr, Mo, W, Nb, and Ta) contributes to modulating the adsorption energies of *O and *OH, thereby reducing the overpotential.[13,14,16,27,28,32] In this context, high-entropy alloys of active Fe, Co, and Ni with transition metals (Mo, W) were prepared for AEMWE. The high entropy alloy FeCoNiMoW exhibited excellent OER performance after reconstruction. Mo and W components as the sacrificial agent were etched in the reconstruction to generate the core–shell structure with a FeCoNiOOH-enriched shell. Besides, the reconstruction generated more oxygen vacancies and facilitated the formation of active M-OOH species. After reconstruction, the high-valent metals Mo and W acted as electron donors to maintain the surface active metal sites in the OER process. Therefore, this core–shell catalyst exhibited excellent OER performance with a low overpotential of only 246 mV@10 mA cm^{-2} in 1 M KOH electrolyte and excellent stability of 1000 h at 100 mA cm^{-2}. Moreover, this catalyst also displayed a very low voltage of only 1.74 V to reach 1 A cm^{-2} current in AEMWE and a durability of 430 h@1 A cm^{-2} with a decay rate of only 0.023 mV h^{-1}.

2. Experimental

2.1 Materials

Iron(III) chloride ($FeCl_3$, AR, FW: 162.5) purchased from Meryer (Shanghai) Chemical Technology Co., Ltd. Cobalt(II) chloride ($CoCl_2$, 92.5%, FW: 129.83) and nickel(II) chloride ($NiCl_2$, Ni > 42%) was purchased from Shanghai Titan Technology Co., Ltd. Molybdenum(V) chloride ($MoCl_5$, 95%, FW: 273.23) and tungsten(VI) chloride (WCl_6, 99%, FW: 396.56) were purchased from Aladdin Holdings Group Co., Ltd. Ruthenium dioxide (RuO_2, 99%) were purchased from Anhui Zesheng Technology Co., Ltd. Carbon fiber paper (TGP-H-060) purchased from Incole Union (Tianjin) Chemical Technology Co., Ltd. Potassium hydroxide (KOH, GR) was bought from Aladdin Holdings Group Co., Ltd. Ethanol (C_2H_5OH, >99.7%) was purchased from Jiangtian Chemical Co., Ltd. All reagents were used as received. The ultrapure water with a resistivity of 18.2 MΩ cm was used in all experiments.

2.2 Carbothermal shock synthesis of high entropy alloy catalysts

An equimolar mixture of the chloride precursors was first prepared with the proportion: $FeCl_3$ (1.63 g), $CoCl_2$ (1.30 g), $NiCl_2$ (1.30 g), $MoCl_5$ (2.73 g), WCl_6 (3.94 g). The precursors were

mixed in a ball mill jar at a frequency of 50 Hz for 3 minutes. Then, the mixed powder was put into the Joule heater. The chamber was closed, argon gas was introduced, and the tail gas valve was opened to circulate the argon gas. The rapid heating mode was selected with a temperature of 1127 °C for 20 seconds. At the end of the heating process, the sample was removed. The collected powder was centrifuged with deionized water and dried at 120 °C for 6 h. The dried sample was labeled as FeCoNiMoW. Similarly, the samples of FeCoNiW, FeCoNiMo, FeCoNi, and MoW were synthesized in the same method.

2.3 Preparation of HEA-FeCoNiMoW/CFP electrocatalysts

The carbon fiber paper (1 cm × 1.5 cm) was pretreated in 0.5 M H_2SO_4 under ultrasonication for 30 min and was washed with ultra-pure water to remove the surface acid. Then, 10 mg of the as-synthesized alloy powder was dissolved in a solution containing 600 μl ethanol, 300 μl ultra-pure water, and 100 μl Nafion. The obtained mixture was ultrasonicated for 1.5 h to form uniform ink. Finally, 330 μl of the ink solution was coated onto the pretreated carbon paper with a 1 × 1 cm^2 area and dried to obtain the HEA-FeCoNiMoW/CFP electrocatalyst.

2.4 Preparation of FeCoNiMoW@FeCoNiOOH/CFP catalysts by *in situ* reconstruction

The HEA-FeCoNiMoW/CFP electrocatalyst was reconstructed by cyclic voltammetry (CV) using Hg/HgO as the reference electrode and platinum mesh as the counter electrode in a typical three-electrode system before the test. The scanning was performed at a rate of 20 mV s^{-1} within the potential range of 1.124–1.724 V *vs.* RHE for 300 cycles. The reconstructed catalyst was named FeCoNiMoW@FeCoNiOOH/CFP. Similarly, the HEA-FeCoNiW/CFP and other samples were also treated in the same CV method, and named HEA-FeCoNiW/CFP@EA (electrochemical activation), HEA-FeCoNiMo@EA, MEA-FeCoNi@EA, and MoW@EA, respectively.

2.5 Catalyst characterizations

The X-ray diffraction data were obtained using a German Bruker X-ray diffractometer (D8 Focus) for analyzing the crystal phase structure of the prepared electrocatalyst. Cu target Kα rays (λ = 0.154 nm) were used, with a scanning angle range of 20°–80° and a scanning rate of 5° min^{-1}. The morphology of the catalyst was analyzed using field emission scanning electron microscopy Apreo S LoVac (FE-SEM) with an acceleration voltage of 15 kV. The elemental mapping was collected to analyze the distribution of element species in a wide range. The microstructure, structure, particle size, and lattice fringes of the catalyst were characterized using a JEM-F200 field emission transmission electron microscope (TEM). At the same time, the types and distributions of elements, relative contents, and crystalline states of the catalyst were obtained through energy dispersive electron spectroscopy (EDS) and selected area electron diffraction (SAED). The surface elemental composition and valence states of the catalyst were analyzed using K-Alpha + X-ray photoelectron spectroscopy (XPS), and the binding energy of the sample was corrected using the C 1s (284.8 eV). The molecular structure of the catalyst was characterized and analyzed using an inVia Reflex RENISHAW laser Raman spectrometer. A neodymium-doped yttrium aluminum garnet laser with a wavelength of 532 nm was used, with a wavenumber range of 200–1000 cm^{-1}. The Agilent 730 series inductively coupled plasma optical emission spectrometer (ICP-OES) was used to measure the composition of electrocatalysts and the content of leached metals in electrolytes. The oxygen vacancies of the catalysts were tested using an electron paramagnetic resonance spectrometer EPR (Bruker EMXPlus, A300).

2.6 Electrochemical measurements

The electrochemical activity tests were carried out in a three-electrode system using an Autolab PGSTAT302 electrochemical workstation in 1 M KOH electrolyte with the as-prepared electrodes as the working electrode, platinum mesh as the counter electrode, and Hg/HgO electrode as the reference electrode. All tests were conducted at a constant temperature of 30 °C. The potential was converted to the reversible hydrogen electrode (RHE) using the formula $E_{RHE} = E_{Hg/HgO} + 0.059^{*}$ pH + 0.098 V. The test results have been compensated with 95% *iR*. Then, the activity evaluation was conducted in the potential range of 1.094–2.004 V *vs.* RHE with a scan rate of 5 mV s^{-1}. The electrochemical impedance spectrum (EIS) was obtained at a potential of 0.56 V *vs.* Hg/HgO in the frequency range of 100 kHz to 0.01 Hz. The CV scans were performed in the range of 0.36 to 0.46 V *vs.* Hg/HgO at a series of scan rates with 20, 40, 60, 80, and 100 mV s^{-1} to calculate the double-layer capacitance (C_{dl}). Additionally, the catalyst stability test was performed using the chronopotentiometry method to test the durability of the catalyst at a current density of 100 mA cm^{-2}.

2.7 Evaluation of anion exchange membrane water electrolysis (AEMWE)

The FeCoNiMoW@FeCoNiOOH/CFP catalyst and PtRu/C were dispersed ultrasonically in a mixture of PiperION-A5 ionomer (mass ratio of ionomer/catalyst was 0.2) and a solvent mixture of isopropanol and water (3 : 1 v/v) to form a homogeneous catalyst ink. The catalyst inks were sprayed onto the gas diffusion layers (GDLs) (2 × 2 cm^2; anode, stainless steel felt; cathode, TGP-H-060 carbon paper) with a mass loading of ~1.0 mg cm^{-2}. The PiperION-A40R-HCO3 membrane was immersed in 1 M KOH solution for 12 h. After that, the electrolytic cell was assembled with GDL and Teflon pads. The electrolyzer was tested by a PTC-05100EW electrochemical workstation combined with a DC power supply (IT6723C). A 1 M KOH solution was flowed on the anode and cathode at 60 °C prior to testing and a CV test (1.2–2.0 V) was applied to activate the cells until the polarization curves stabilized and then the polarization curves were recorded at a scan rate of 10 mV s^{-1}. The electrochemical impedance of the anion exchange membrane water electrolysis cell was tested at a constant current of 1 A cm^{-2}, with a scanning frequency range of 100 kHz–1 Hz.

3. Results and discussion

3.1 Texture structure and chemical state of FeCoNiMoW@FeCoNiOOH/CFP catalysts

The morphology and structure of the as-synthesized electrocatalysts were characterized by field emission scanning electron microscopy (SEM). The HEA-FeCoNiMoW/CFP had a non-uniform particle size distribution and showed an interconnected three-dimensional porous skeletal structure (Fig. 1b and c). This 3D structure was expected to have a better OER performance. The element contents were determined by ICP-OES. The HEA-FeCoNiMoW/CFP catalyst consisted of 21.91% Fe, 9.67% Co, 7.04% Ni, 30.55% Mo, and 30.83% W. The higher contents of Mo and W indicated that these two metals were more accessible to the alloy by carbon thermal shock, while the active element Ni was suppressed. Each elemental proportion was between 5%~35%, and the entropy of the catalyst mixture was 1.51*R*, suggesting the successful synthesis of a high entropy alloy.[30,33–36] After the electrochemical self-reconstruction, the smaller particles were obtained and uniformly distributed on the surface (Fig. 1d and e). This further increased the specific surface area of the catalyst and facilitated the exposure of the active sites.

To further probe the atomic structure of the HEA-FeCoNiMoW/CFP and FeCoNiMoW@FeCoNiOOH/CFP catalysts, an aberration-corrected high-angle annular dark field scanning transmission electron microscope (HAADF-STEM) was used. The HEA-FeCoNiMoW/CFP catalyst

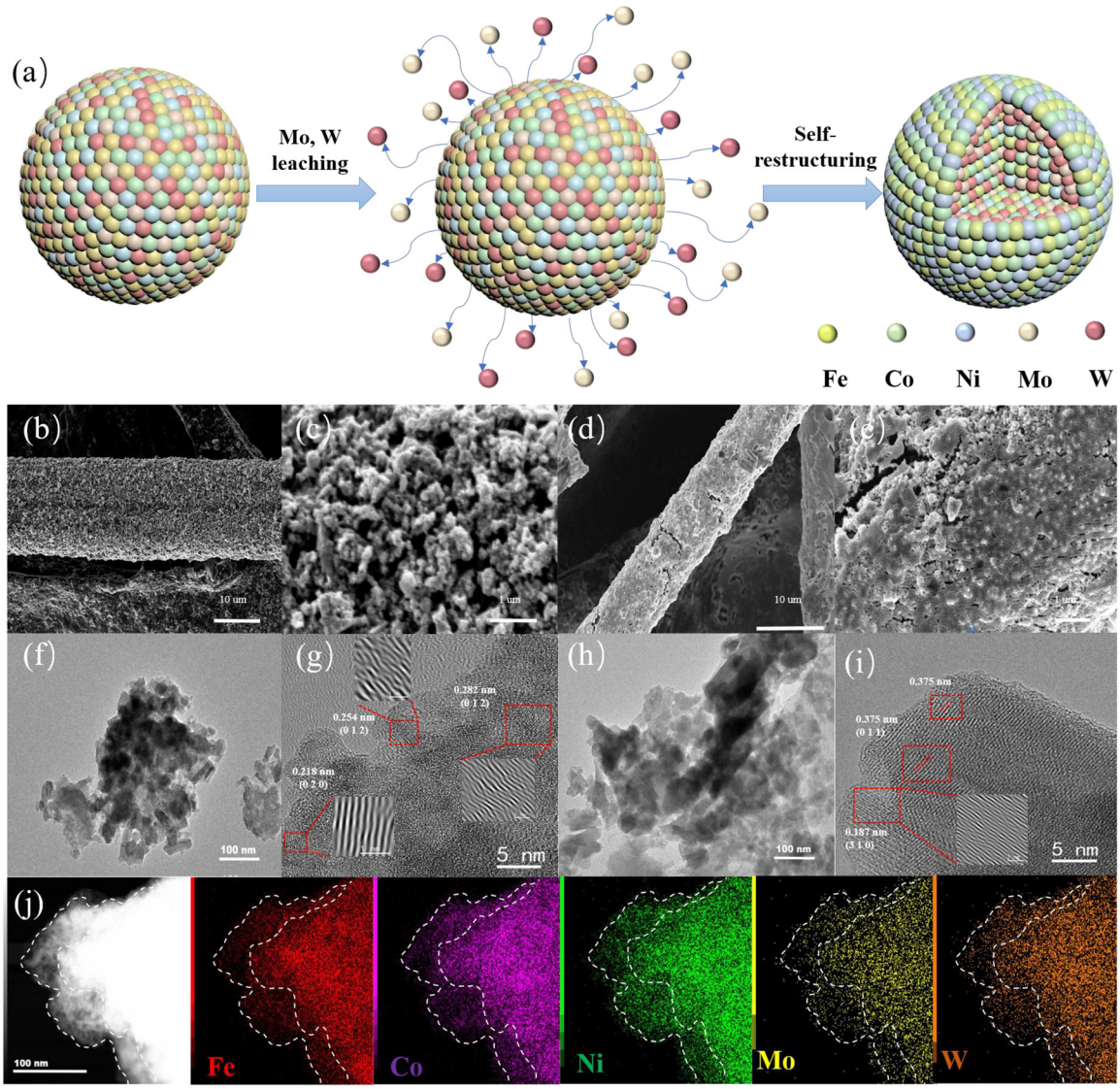

Fig. 1 Morphology and structure of HEA-FeCoNiMoW/CFP, FeCoNiMoW@FeCoNiOOH/CFP electrodes. (a) Schematic illustrations of the core/shell FeCoNiMoW@FeCoNiOOH/CFP nanospheres. (b and c) SEM image of HEA-FeCoNiMoW/CFP, (d and e) SEM image of FeCoNiMoW@FeCoNiOOH/CFP, (f and g) TEM and HRTEM images of HEA-FeCoNiMoW/CFP, (h and i) FeCoNiMoW@FeCoNiOOH/CFP, (j) EDX Mapping of FeCoNiMoW@FeCoNiOOH/CFP Fe, Co, Ni, Mo, and W.

still exhibited an inhomogeneous particle size distribution with the lattice space of 0.218 nm belonging to the (020) crystal plane of $FeWO_4$ (JCPDS No. 46-1446), indicating the presence of Fe and W alloy oxide in HEA (Fig. 1f and g). The crystals showed an interplanar spacing of 0.252 nm, corresponding to the (311) plane of $NiFe_2O_4$ (JCPDS No. 10-0325). This indicated the presence of Fe–Ni alloy oxides in HEA (Fig. 1f and g). These results further proved the synthesis of alloy oxides. After *in situ* reconstruction, the catalysts exhibited a clear core–shell structure with a thick center and thin edges (Fig. 1j). The XPS results showed that the Mo and W contents in the thin edges were greatly reduced, and the generated thin shell was composed of 19.14% Fe, 37.33% Co, 36.39% Ni, 3.38% Mo, and 3.76% W, respectively. The mixing entropy of the shell layer was calculated to be 1.29*R*, suggesting that the shell was composed of a medium-entropy alloy. The TEM line scanning image further confirmed the formation of this core–shell structure (Fig. S2†). Interestingly, a new lattice fringe of 0.375 nm was observed (Fig. 1h and i), which was ascribed to (Co, Ni)O(OH) (JCPDS No. 29-0491), indicating the formation of M-OOH active species after reconstruction. In addition, a new planar spacing of 0.187 nm also appeared, which was attributed to the (310) crystal faces of FeOOH. This demonstrated that FeOOH was produced in the reconstructed catalyst.[37] These suggested that a core–shell alloy structure with the FeCoNiOOH-enriched medium entropy alloy shell and HEA-FeCoNiMoW core was fabricated after reconstruction. The formation of M-OOH active species was beneficial for enhancing the activity of the catalyst.

The crystal structures of the as-prepared samples were analyzed by X-ray diffraction and Raman characterization. The X-ray diffraction (XRD) patterns of the resulting catalysts showed very weak diffraction peaks (Fig. 2a), indicating that these catalysts were mainly in an amorphous phase. The Raman patterns of FeCoNiMoW@FeCoNiOOH/CFP showed three peaks at 467 cm^{-1}, 548 cm^{-1}, and 667 cm^{-1}, corresponding to Ni/Co-OOH and Fe-OOH, respectively.[38] However, the HEA-FeCoNiMoW/CFP did not show any peaks in these ranges, suggesting that this catalyst did not contain hydroxyl oxides before reconstruction. These results provided strong evidence for the formation of hydroxyl peroxide species on the HEA surface after *in situ* electrochemical self-reconstruction. In order to explore the reconstruction process, *in situ* Raman characterization was performed during the OER process in 1 M KOH solution (Fig. 2c). The HEA precursor mainly exhibited the peaks of oxides at the OCP potential. As the potential rises, the oxide peaks fade away, and new peaks assigned to M-OOH species gradually appear. The increasing intensity of the

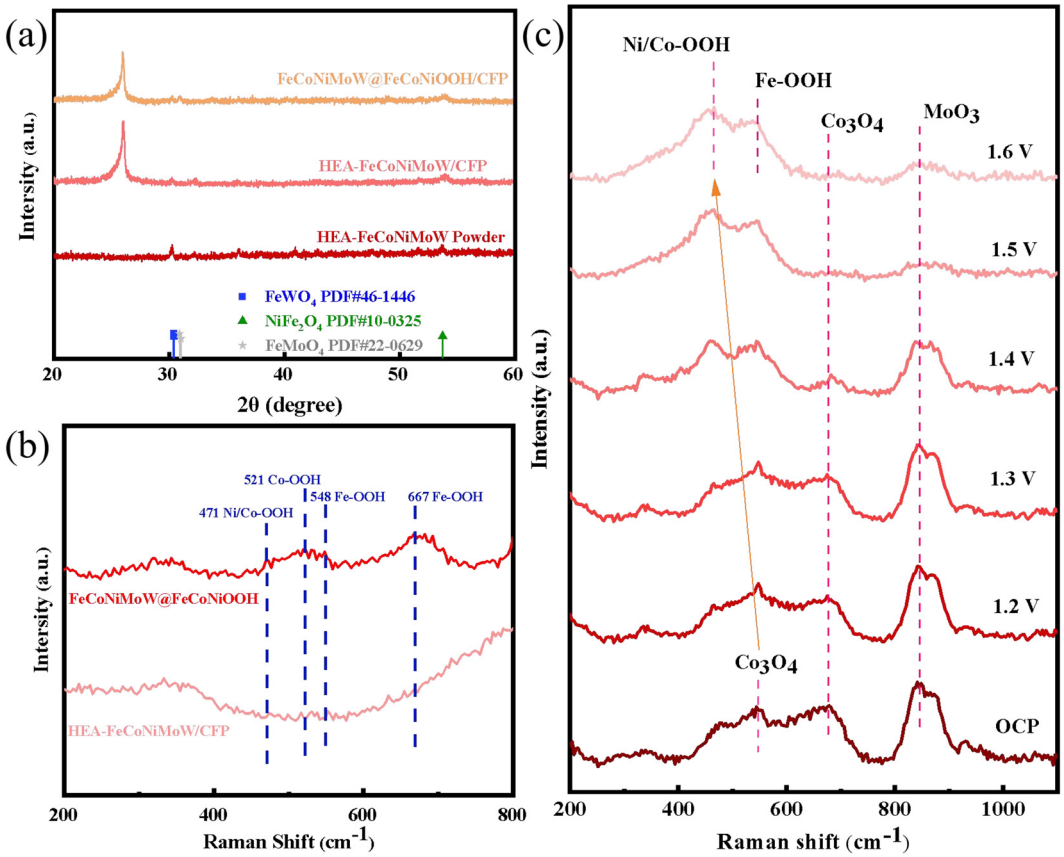

Fig. 2 XRD and Raman. (a) XRD pattern of HEA-FeCoNiMoW powder, HEA-FeCoNiMoW/CFP, and FeCoNiMoW@FeCoNiOOH/CFP; (b) Raman spectrum of the HEA-FeCoNiMoW/CFP and FeCoNiMoW@FeCoNiOOH/CFP; (c) *in situ* Raman plot of HEA-FeCoNiMoW/CFP.

M-OOH peak at 467 cm^{-1} was attributed to the bending and stretching vibrations of Ni(III)-O in γ-NiOOH.[39] The peaks of the Ni species varied with the potential increase, suggesting the occurrence of a surface reconstruction process. These results further proved the formation of M-OOH species on the surface of reconstructed catalysts. Besides, the initial potential to form the M-OOH peaks for HEA-FeCoNiMoW/CFP was much lower than MEA-FeCoNi/CFP (1.2 V_{RHE} *vs.* 1.4 V_{RHE}). This indicated that the leaching of Mo and W promoted the rapid self-reconstruction of the HEA-FeCoNiMoW/CFP catalysts (Fig. S3†).

The electronic structure and elemental valence states of the catalysts before and after electrochemical reconstruction were investigated by XPS technology (Fig. 3). The Fe 2p XPS spectra of HEA-FeCoNiMoW/CFP presented several peaks at 707.1 eV, 711.7 eV, 722.5 eV, 715.1 eV, and 725.5 eV, which were attribu-

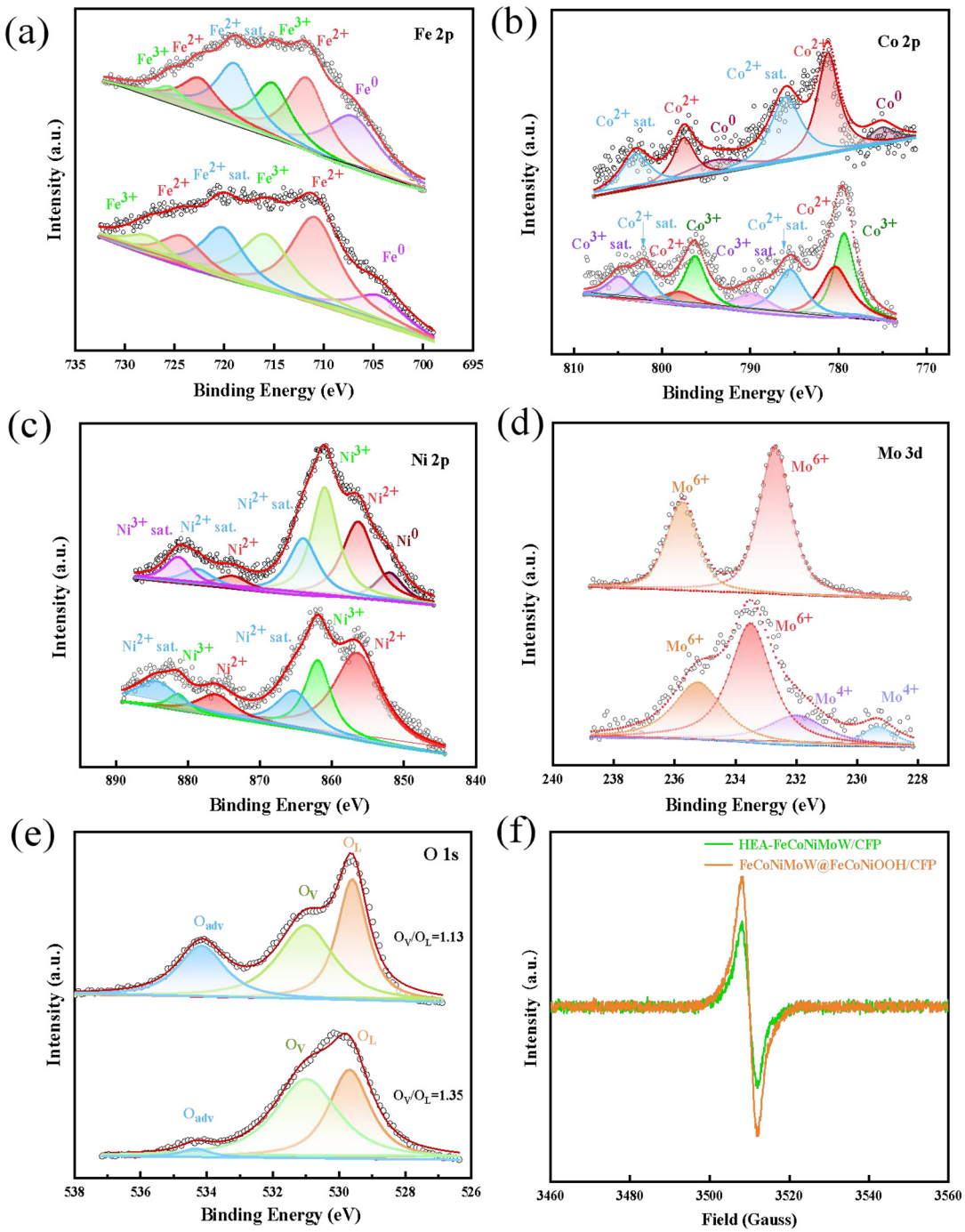

Fig. 3 XPS spectra of HEA-FeCoNiMoW/CFP (top) and FeCoNiMoW@FeCoNiOOH/CFP (bottom). (a) Fe 2p; (b) Co 2p; (c) Ni 2p; (d) Mo 3d; (e)O 1s; (f) electron paramagnetic resonance spectroscopy of HEA-FeCoNiMoW/CFP and FeCoNiMoW@FeCoNiOOH/CFP.

ted to Fe^0 $2p_{1/2}$, Fe^{2+} $2p_{3/2}$, Fe^{2+} $2p_{1/2}$, Fe^{3+} $2p_{3/2}$, and Fe^{3+} $2p_{1/2}$, respectively.[40,41] The Co 2p spectra showed two pairs of peaks at 774.0 eV and 794.0 eV, 782.1 eV and 797.5 eV, which were ascribed to Co^0 $2p_{3/2}$, Co^0 $2p_{1/2}$ and Co^{2+} $2p_{3/2}$, and Co^{2+} $2p_{1/2}$, respectively. The Ni 2p XPS spectra exhibited two spin–orbit peaks at 852.0 eV, 855.9 eV, and 873.8 eV corresponding to the Ni^0 and Ni^{2+} species, respectively. For the Mo 3d spectra, the peaks at 235.7 eV and 232.7 eV were assigned to the Mo^{6+} species of Mo $3d_{3/2}$ and Mo $3d_{5/2}$, respectively.[42,43] Besides, the W 4f XPS spectra showed two obvious peaks at about 35.7 eV and 34.0 eV, assigned to the W^{6+} species (Fig. S4†).[40,44] These results indicated that the metals in HEA-FeCoNiMoW/CFP mainly existed in the oxidation state, suggesting it to be a high-entropy alloy oxide.

After self-reconstruction, the Fe^{3+}/Fe^{2+} ratio increased significantly, suggesting that Fe-OOH species might be produced. In the Co 2p XPS spectra, two new peaks appeared at 780.2 eV and 789.9 eV corresponding to Co^{3+} $2p_{3/2}$ and Co^{3+} $2p_{1/2}$ with the disappearance of Co^0 species. This could be attributed to the oxidation of Co into active CoOOH species in the reconstruction process.[35,45] Simultaneously, the Ni^0 species peak disappeared, and the binding energies of Ni^{2+} $2p_{3/2}$ shifted towards a higher one by 0.1 eV, suggesting the formation of NiOOH.[31,42] Mo^{4+} species also appeared except for Mo^{6+}, indicating that the partial reduction occurred to enhance the electron density of Mo metal. In addition, the ratio of W^{6+} /W^{5+} peak area was significantly reduced, indicating that part of W^{6+} was transformed to W^{5+}. These results further indicated that after reconstruction, the Fe/Co/Ni species were further oxidized into higher valence species M-OOH, but Mo and W were present in an electron-rich state. This was in agreement with that of Raman spectroscopy. These results further confirmed that the surface FeCoNi were oxidized into active Fe-OOH, Ni-OOH, and Co-OOH species after the self-reconstruction, while the Mo and W species, mainly in the core partially reduced into lower valence and acted as the electron reservoir.

Besides, the O 1s XPS spectra were also analyzed (Fig. 3e). The spectrum curves were fitted with three peaks at 529.5, 530.8, and 535.1 eV, which belonged to lattice oxygen (O_L), oxygen vacancies (O_v), and adventitious species (O_{adv}), respectively.[34,46,47] The ratio of O_V/O_L was used to estimate the number of oxygen vacancies on the surface. The ratio changed from 1.13 to 1.35 after reconstruction. The proportion of oxygen vacancies was significantly increased for the FeCoNiMoW@FeCoNiOOH/CFP. To further explore the oxygen vacancies, EPR was used to reveal changes in the oxygen vacancies (Fig. 3f).[48,49] It showed that the sample displayed a strong symmetric EPR signal at $g = 2.002$, which suggested that the oxygen vacancy content increased after reconstruction. This was consistent with the change in the ratio of O_V/O_L for O 1s in XPS. This might be attributed to the etching of Mo and W to generate more oxygen vacancies on the reconstructed

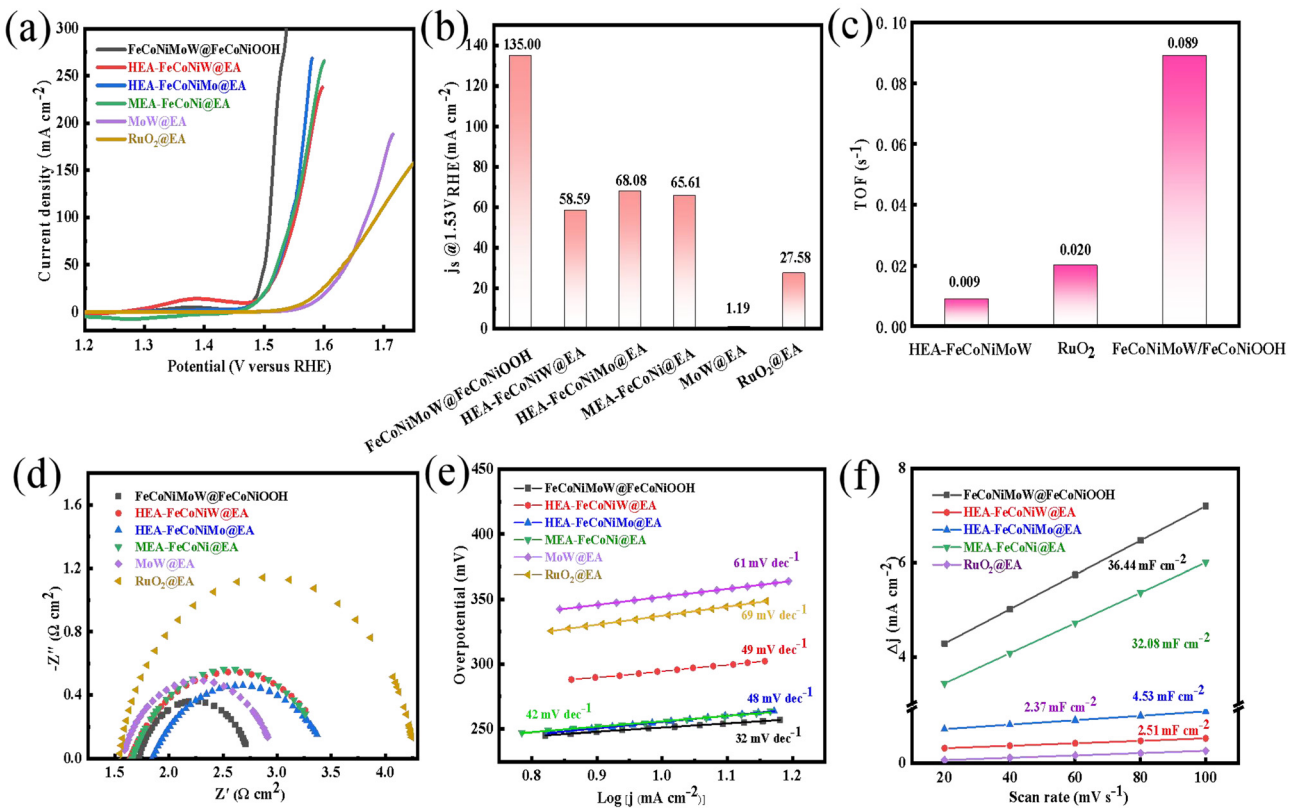

Fig. 4 Electrochemical OER performance. (a) LSV curves, (b) specific activity, (c) turnover frequency, (d) Tafel plots, (e) electrochemical impedance spectroscopies, (f) double layer capacitance (C_{dl}) by CV scans.

surface.[47] As reported, the vacancies not only helped to tune the electronic structure but also favored the exposure of active sites.[19,50]

3.2 Electrocatalytic OER performance

The electrochemical properties of all electrode materials were tested in 1 M KOH electrolyte using a standard three-electrode cell with HEA catalysts as the working electrodes, Pt mesh as the counter electrode, and Hg/HgO as the reference electrode. FeCoNiMoW@FeCoNiOOH/CFP exhibited excellent performance with a low overpotential of 246 mV to achieve the current density of 10 mA cm^{-2}, a high current density of 135 mA cm^{-2}@1.53 V_{RHE}, and a TOF value (0.089 s^{-1}) (Fig. 4a–c). Moreover, the current density at 1.53 V_{RHE} and TOF values were 4.9 and 4.6 times higher than commercial RuO_2 and also surpassed most of the reported HEA electrocatalysts. This could be attributed to the good synergistic effects of the five-membered high-entropy alloy and the formation of a highly active M-OOH enriched surface in FeCoNiMoW@FeCoNiOOH/CFP catalyst. To verify the role of synergistic effects between different components in HEA (Fig. 4a), the FeCoNiW/CFP@EA (258 mV), HEA-FeCoNiMo/CFP@EA (257 mV), MEA-FeCoNi/CFP@EA (256 mV), and MoW/CFP@EA (361 mV) were evaluated, suggesting that the Mo and W independently composites with FeCoNi exhibit the un-affected activity of FeCoNi. These results imply that the strong synergistic effects of five-membered high-entropy alloy enhanced the activity of FeCoNiMoW@FeCoNiOOH/CFP catalyst. The overpotential of the FeCoNiMoW@FeCoNiOOH/CFP catalyst was reduced by 40 mV compared with that of the catalysts before reconstruction (HEA-FeCoNiMoW) (Fig. S5†), and the TOF value of FeCoNiMoW@FeCoNiOOH/CFP was 10 times as high as that of HEA-FeCoNiMoW (0.009 s^{-1}). This indicated that the core–shell structure with a surface enriched in highly active M-OOH also contributed to improving the catalytic activity. Besides, FeCoNiMoW@FeCoNiOOH/CFP also exhibited the smallest Tafel slope (32 mV dec^{-1}), indicating the fastest OER kinetics on its surface (Fig. 4e). The charge transfer resistance of this

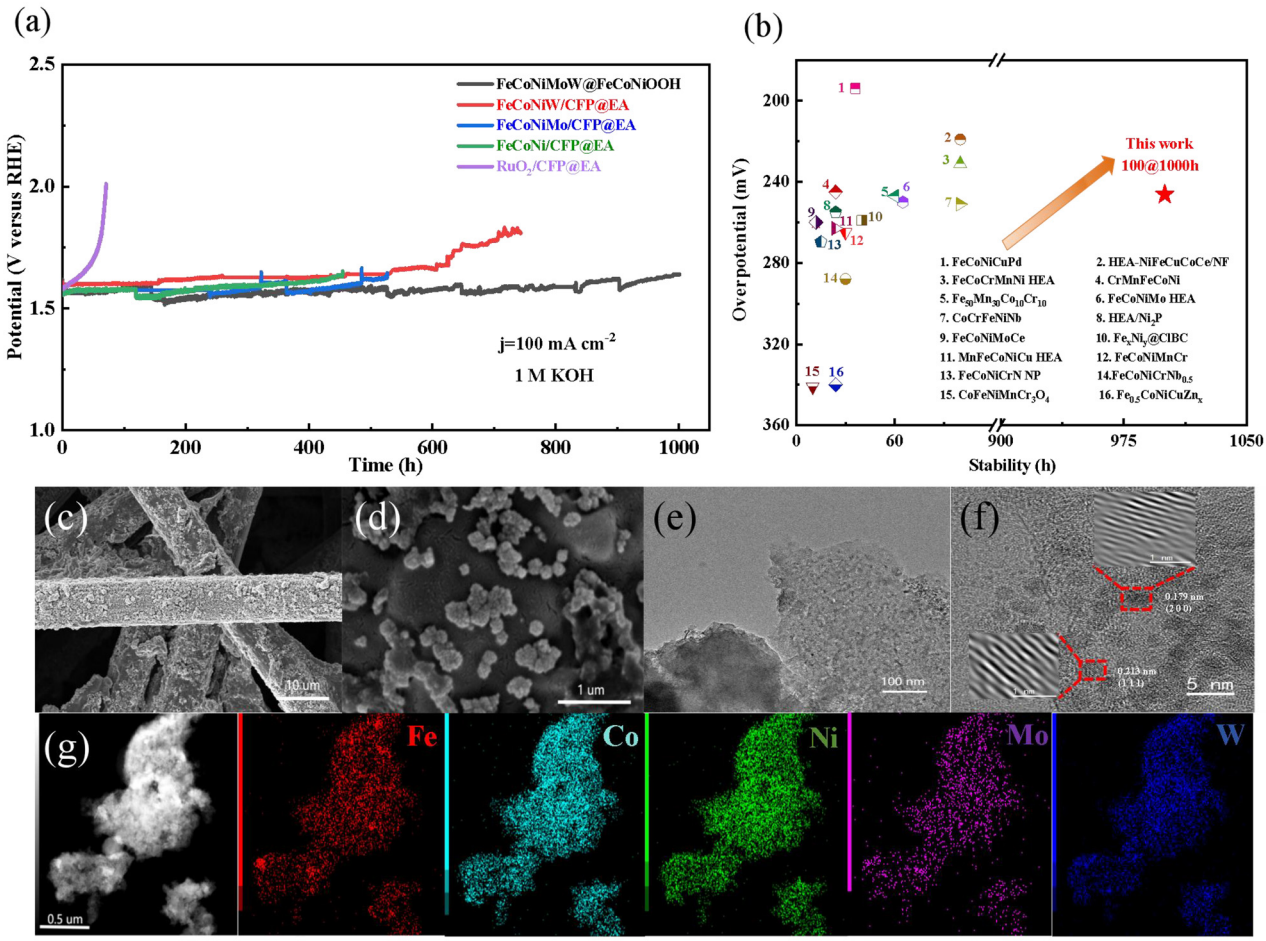

Fig. 5 Stability test. (a) The chronopotentiometry measurement of FeCoNiMoW@FeCoNiOOH/CFP, HEA-FeCoNiW/CFP@EA, HEA-FeCoNiMo/CFP@EA, MEA-FeCoNi/CFP@EA, and commercial RuO_2/CFP@EA in 1 M KOH, (b) the comparison of both overpotential at 100 mA cm^{-2} and stability for OER with references all measured in alkaline media. (c) Low- and (d) high-magnification SEM images of FeCoNiMoW@FeCoNiOOH/CFP after stability test, (e) TEM image and (f) HRTEM image of FeCoNiMoW@FeCoNiOOH/CFP after stability test, (g) EDS elemental mappings of FeCoNiMoW@FeCoNiOOH/CFP after stability test.

catalyst was also determined by EIS. FeCoNiMoW@FeCoNiOOH/CFP showed the smallest charge transfer resistance of 1.58 Ω compared with the catalysts of HEA-FeCoNiW/CFP@EA (1.87 Ω), HEA-FeCoNiMo/CFP@EA (1.64 Ω), and MEA-FeCoNi/CFP@EA (1.80 Ω), and commercial RuO_2/CFP@EA (2.74 Ω), further supporting the enhanced FeCoNiMoW@FeCoNiOOH/CFP kinetics (Fig. 4d). Moreover, the electrochemically active surface area of the HEA catalyst was estimated by measuring the double-layer capacitance through cyclic voltammetry within a suitable potential range. Fig. 4(f) showed that FeCoNiMoW@FeCoNiOOH/CFP had the largest double-layer capacitance (36.44 mF cm^{-2}), suggesting that FeCoNiMoW@FeCoNiOOH/CFP could expose much more active sites than its precursor HEA-FeCoNiMoW. These results indicated that the core–shell FeCoNiMoW@FeCoNiOOH/CFP electrocatalysts exhibited a large electrochemically active surface area, the ultralow Tafel slope, and low charge transfer resistance to boost the OER performance.

3.3 Long-term stability evaluation

In addition to the electrocatalytic activity, the stability of the catalyst was essential for evaluating the catalysts, especially at high current densities.[51] The FeCoNiMoW@FeCoNiOOH/CFP showed an excellent stability of 1000 h at 100 mA cm^{-2} with a very slight increase of the overpotential (*ca.*21 mV), which was 16.5 times higher than commercial RuO_2 (Fig. 5a). While the

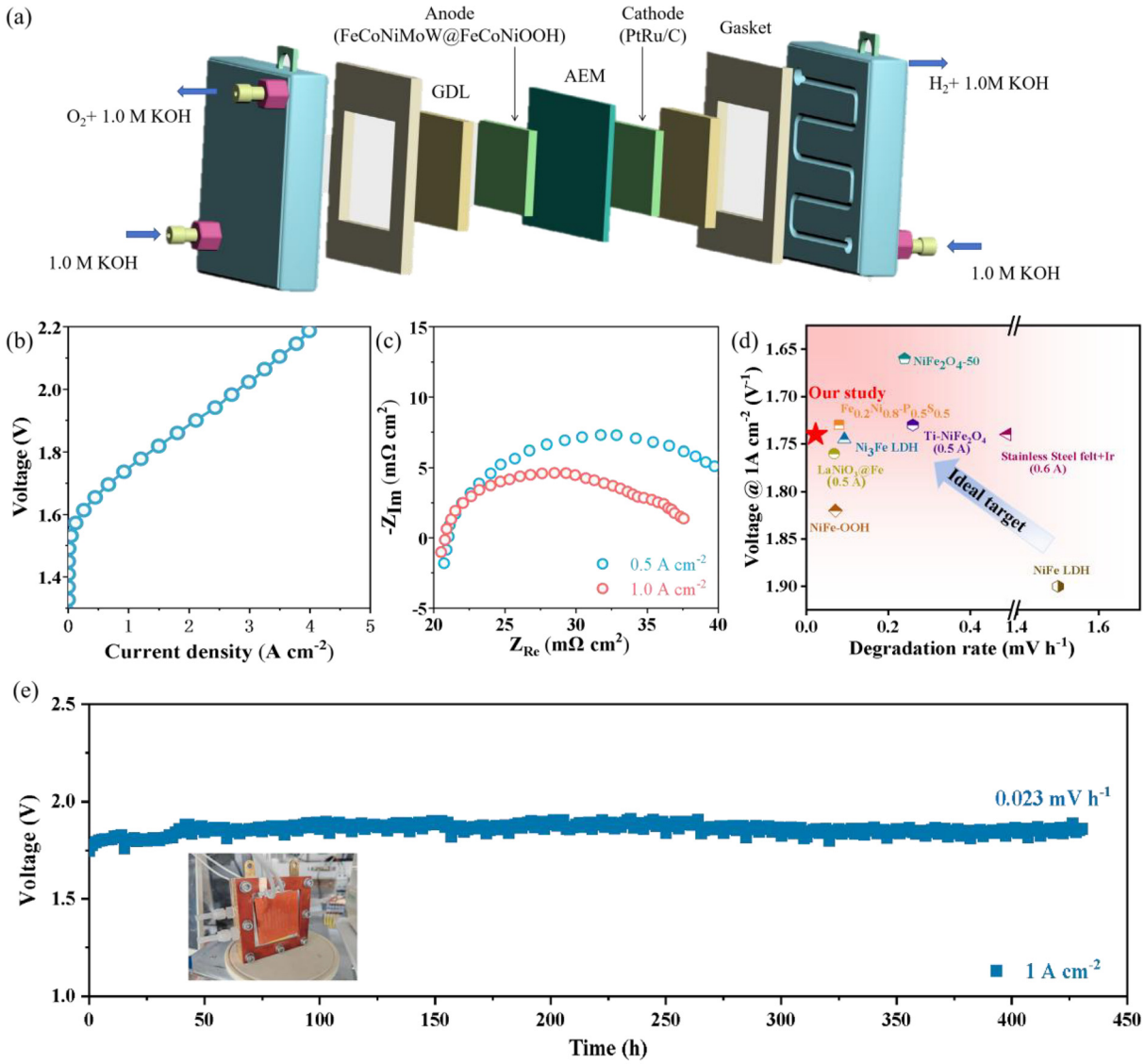

Fig. 6 AEMWE performance. (a) Schematic illustration of AEMWE single-cell configuration, (b) polarization curves of the AEMWE obtained at 60 °C with PiperION-A40-HCO3 membrane, (c) electrochemical impedance spectroscopies, (d) comparison of the performance and degradation rates of the state-of-the-art AEMWE systems using non-noble metal-based anodes during the long-term durability test, (e) chronopotentiometry curves of the AEM electrolyzer with FeCoNiMoW@FeCoNiOOH and 60% PtRu/C electrocatalysts operated at 1.0 A cm^{-2}. The inset image in (e) is a photograph of the components of the designed AEMWE cell.

HEA-FeCoNiW/CFP@EA and HEA-FeCoNiMo/CFP@EA could remain stable for only 610 h and 520 h@100 mA cm^{-2}, respectively. But the Mo and W-free MEA-FeCoNi/CFP@EA catalyst could only work stably for 440 h. These indicated that the enhancement of stability could be attributed to the synergistic effect of the core–shell structure by leaching the surface Mo and W. The slight fluctuation might be caused by the aggregation and diffusion of O_2 bubbles on the surface during the OER process, as well as the leaching of the electrocatalyst from the surface of the electrodes. The stability of this reconstructed catalyst was also superior to other similar catalysts reported recently (Fig. 5b). In order to further investigate the structural stability of the FeCoNiMoW@FeCoNiOOH/CFP electrode, a series of characterizations were carried out after long-term durability. Inductively coupled plasma mass spectrometry (ICP-MS) was used to detect the content of leaching elements in the electrolyte after the long-term stability test (Table S2†). Each element in the FeCoNiMoW@FeCoNiOOH/CFP was slightly dissolved with relatively more Mo and W. The low dissolution rate of the FeCoNiMoW@FeCoNiOOH/CFP high-entropy alloy catalyst further suggested excellent structure stability, which was attributed to the high corrosion resistance of the formation of a highly durable core–shell structure. The morphology of these electrocatalysts remained almost intact after a long-term durability test. Similar TEM images with the characteristic indications of initial FeCoNiMoW@FeCoNiOOH/CFP were obtained, indicating the excellent stability of the core–shell structure. The chemical and electronic states of the FeCoNiMoW@FeCoNiOOH/CFP after long-term testing were also characterized by XPS (Fig. S5†). No significant changes were observed in the peaks of Ni 2p, Fe 2p, and Co 2p compared to the initial catalyst. The highly active surface enriched in Ni/Fe/Co-OOH species was well maintained. The proportion of low-valence Mo to W obviously increases, indicating that more Mo and W species in the electron-rich state were generated. This suggested that Mo and W acted as the electron reservoir in the OER process, which could enhance the electron transfer to the adjacent active sites, Fe/Co/Ni-OOH, to inhibit their overoxidation. Therefore, the special core–shell structure realized the win-win strategy of high activity and high stability. The catalyst surface elemental composition was characterized before and after the stability test using XPS, which showed little change in the catalyst surface elemental composition, further indicating the high stability of the catalyst shell layer.

3.4 Performance and durability of the AEMWE

In order to further evaluate the feasibility of electrocatalysts for practical applications, an anion exchange membrane water electrolyzer (AEMWE) was assembled using a membrane-electrode-assembly (MEA) with the FeCoNiMoW@FeCoNiOOH catalyst as the anode and 60% PtRu/C as the cathode (Fig. 6a). The electrolyzer was then tested in 1 M KOH solution at 60 °C. FeCoNiMoW@FeCoNiOOH||PtRu/C MEA required only 1.74 V_{cell} and 2.18 V_{cell} to reach the high current densities of 1 A cm^{-2} and 4 A cm^{-2}, respectively (Fig. 6b). To further analyze the impact of the electrocatalyst on the AEM electrolyzer, EIS analysis was performed, and Nyquist plots were obtained (Fig. 6c). The radius of the semicircle in the Nyquist plot indicates the polarization resistance of the AEM electrolyzer.[52] The AEM electrolyzer prepared with FeCoNiMoW@FeCoNiOOH showed a smaller EIS radius, and the semicircle at 1 A cm^{-2} current density was smaller than the semicircle at 0.5 A cm^{-2}, which suggested that the kinetics were faster at the high current density of 1 A cm^{-2}. Moreover, the durability of this AEM electrolyzer was also tested at a current density of 1 A cm^{-2}. The cell voltage increased only 0.01 V for 430 h, and the cell degradation was as small as 0.023 mV h^{-1}, confirming its stable activity at a very large operating current (Fig. 6e). The performance of MEA was compared to literature reports (Fig. 6d and Table S7†). The FeCoNiMoW@FeCoNiOOH||PtRu/C MEA required a lower voltage to achieve the current density of 1 A cm^{-2} and had the lowest degradation rate. These results suggested that the FeCoNiMoW@FeCoNiOOH high-entropy alloy electrocatalyst was an efficient and durable anode material for industrial AEM water electrolysis.

4. Conclusion

In summary, a stable core–shell FeCoNiMoW@FeCoNiOOH electrocatalyst was synthesized by *in situ* electrochemical self-reconstruction of FeCoNiMoW high-entropy alloy catalysts. The leaching of Mo and W promoted the formation of FeCoNiOOH-enriched medium entropy alloy shell structure and the active sites MOOH. This core–shell FeCoNiMoW@FeCoNiOOH electrocatalyst exhibited excellent catalytic activities, kinetics, and stability toward OER in an alkaline solution, which could be attributed to the synergistic effects between different components as well as the core–shell structure in five-member HEA. The Mo and W acted as electron donors, enhancing electron transport and providing electrons to the active sites, thus ensuring excellent catalyst durability. Furthermore, the AEM electrolyzer assembled using FeCoNiMoW@FeCoNiOOH MEA also achieved a good performance of superior activity (2.18 V_{cell} at 4 A cm^{-2}) and unprecedented durability (1 A cm^{-2} over 430 h with a slight voltage increase of only 0.01 V) under industrial conditions. This work demonstrated the potential of noble metal-free HEA electrocatalysts in water-splitting devices and provided prospects for the industrial design of electrocatalysts with excellent activity and long-term durability for AEM electrolyzers.

Author contributions

L. G. and Y. H. contributed equally to this work. L. G. and Y. Q. conceived the project. B. C. performed the measurements of the AEMWE. C. L. conducted the investigation. L. G. and Y. H. provided the experimental support. H. C., X. Z., and J. Z. supervised and guided the experiment. Q. W. wrote and reviewed the manuscript.

Conflicts of interest

The authors declare no conflict of interest.

Data availability

The authors confirm that the data supporting the findings of this study are available within the article and ESI.†

Acknowledgements

We acknowledge the funding support from the National Natural Science Foundation of China (21476169) and the National Key Research and Development Program of China (2022YFE0207600).

References

1 S. Wang, A. Lu and C. J. Zhong, *Nano Convergence*, 2021, **8**, 4.
2 H. Yan, Y. Xie, A. Wu, Z. Cai, L. Wang, C. Tian, X. Zhang and H. Fu, *Adv. Mater.*, 2019, **31**, e1901174.
3 Y. Zhang, X. Zhu, G. Zhang, P. Shi and A.-L. Wang, *J. Mater. Chem. A*, 2021, **9**, 5890–5914.
4 Y. Lin, Y. Dong, X. Wang and L. Chen, *Adv. Mater.*, 2023, **35**, e2210565.
5 L. Tian, Z. Li, X. Xu and C. Zhang, *J. Mater. Chem. A*, 2021, **9**, 13459–13470.
6 H. Xu, H. Shang, C. Wang and Y. Du, *Coord. Chem. Rev.*, 2020, **418**, 213374–213394.
7 H. Tuysuz, *Acc. Chem. Res.*, 2024, **57**, 558–567.
8 M.-I. Jamesh, D. Hu, J. Wang, F. Naz, J. Feng, L. Yu, Z. Cai, J. C. Colmenares, D.-J. Lee, P. K. Chu and H.-Y. Hsu, *J. Mater. Chem. A*, 2024, **12**, 11771–11820.
9 Y. Kang, Y. Guo, J. Zhao, B. Jiang, J. Guo, Y. Tang, H. Li, V. Malgras, M. A. Amin, H. Nara, Y. Sugahara, Y. Yamauchi and T. Asahi, *Small*, 2022, **18**, e2203411.
10 X. Zhou, H. Zhu, S. Fu, S. Lan, H. Hahn, J. Zeng and T. Feng, *Small*, 2024, **20**, e2405596.
11 Y. Zhao, X. He, X. Ma, Z. Guo, M. Qi, Z. Liu and R. Tang, *J. Mater. Chem. A*, 2024, **12**, 12077–12087.
12 M. Li, F. Lin, S. Zhang, R. Zhao, L. Tao, L. Li, J. Li, L. Zeng, M. Luo and S. Guo, *Sci. Adv.*, 2024, **10**, eadn2877.
13 Q. Zhang, S. Zhang, Y. Luo, Q. Liu, J. Luo, P. K. Chu and X. Liu, *APL Mater.*, 2022, **10**, 070701.
14 J. Chen, Y. Ling, X. Yu, G. Wang, L. Huang, A. He, Q. Fan, S. Qin, S. Xiang, M. Xu, Z. Han, J. Du and Q. Xu, *J. Alloys Compd.*, 2022, **929**, 167344–167355.
15 C. Cai, Z. Xin, X. Zhang, J. Cui, H. Lv, W. Ren, C. Gao and B. Cai, *Catalysts*, 2022, **12**, 1050.
16 K. Huang, J. Xia, Y. Lu, B. Zhang, W. Shi, X. Cao, X. Zhang, L. M. Woods, C. Han, C. Chen, T. Wang, J. Wu and Y. Huang, *Adv. Sci.*, 2023, **10**, e2300094.
17 Z.-L. Wang, G.-Y. Huang, G.-R. Zhu, H.-C. Hu, C. Li, X.-H. Guan and H.-B. Zhu, *Appl. Catal., B*, 2025, **361**, 124585–124597.
18 S. Wang, B. Xu, W. Huo, H. Feng, X. Zhou, F. Fang, Z. Xie, J. K. Shang and J. Jiang, *Appl. Catal., B*, 2022, **313**, 121472–121485.
19 M. Cui, C. Yang, B. Li, Q. Dong, M. Wu, S. Hwang, H. Xie, X. Wang, G. Wang and L. Hu, *Adv. Energy Mater.*, 2020, **11**, 2002887.
20 Z. Wang, J. Li, S. Yuan, J. Yang, Z. Jin, X. Tan, J. Dang, W. Mu, G. Li and Q. Wang, *Chem. Eng. J.*, 2024, **497**, 154650–154659.
21 S. Qiu, J. Zou, J. Liu, W. Wang, J. Xie, W. Ji, J. Wu, Y. Zhou and Z. Fu, *Small*, 2025, **21**, e2404632.
22 Z.-X. Cai, S. Bolar, Y. Ito and T. Fujita, *Nanoscale*, 2024, **16**, 4803–4810.
23 X. Wang, R. Lu, S. Gong, S. Yang, W. Wang, Z. Sun, X. Zhang, J. Liu and X. Lv, *Chem. Eng. J.*, 2025, **503**, 158488–158500.
24 L. Zhang, W. Cai and N. Bao, *Adv. Mater.*, 2021, **33**, e2100745.
25 L. Sharma, N. K. Katiyar, A. Parui, R. Das, R. Kumar, C. S. Tiwary, A. K. Singh, A. Halder and K. Biswas, *Nano Res.*, 2021, **15**, 4799–4806.
26 Z. Wenyu, G. Ruihua, Y. QuanXin, H. Yarong, Z. GuoFang and G. LiLi, *Ionics*, 2024, **30**, 3403–3416.
27 H. Bian, R. Wang, K. Zhang, H. Zheng, M. Wen, Z. Li, Z. Li, G. Wang, G. Xie, X. Liu and L. Jiang, *Surf. Coat. Technol.*, 2023, **459**, 129407–129417.
28 L. Yi, S. Xiao, Y. Wei, D. Li, R. Wang, S. Guo and W. Hu, *Chem. Eng. J.*, 2023, **469**, 144015–144025.
29 Q. Wang, Y. Qin, J. Xie, Y. Kong, Q. Sun, Z. Wei and S. Zhao, *Adv. Mater.*, 2025, **37**, e2420173.
30 C. Duan, H. Zhang, Z. Hu, Z. Li, W. Bian, C. Jing, J.-Q. Wang and L. Zhang, *J. Mater. Chem. A*, 2025, **13**, 5336–5345.
31 P.-S. Jhu, C.-W. Chang, C.-C. Cheng, Y.-C. Ting, T.-Y. Lin, F.-Y. Yen, P.-W. Chen and S.-Y. Lu, *Nano Energy*, 2024, **126**, 109703–109715.
32 L. Han, S. Dong and E. Wang, *Adv. Mater.*, 2016, **28**, 9266–9291.
33 X. Liang, K. Xu, W. Gao, J. Liang, T. Lv, H. Zhang, J. Lu, L. Zou and J. Liu, *J. Mater. Chem. A*, 2024, **12**, 22030–22036.
34 X. Han, G. Wu, S. Zhao, J. Guo, M. Yan, X. Hong and D. Wang, *Matter*, 2023, **6**, 1717–1751.
35 J. Liang, G. Cao, M. Zeng and L. Fu, *Chem. Soc. Rev.*, 2024, **53**, 6021–6041.
36 R. Xing, X. Wang, G. Wang, Z. Lu, X. Yang, H. Wang, Y. He, X. San, X. Liang and V. A. L. Roy, *Nanoscale*, 2025, 9374–9379.
37 H. Bian, P. Qi, G. Xie, X. Liu, Y. Zeng, D. Zhang and P. Wang, *Chem. Eng. J.*, 2023, **477**, 147286–147296.
38 Y. Duan, Z. Y. Yu, S. J. Hu, X. S. Zheng, C. T. Zhang, H. H. Ding, B. C. Hu, Q. Q. Fu, Z. L. Yu, X. Zheng, J. F. Zhu, M. R. Gao and S. H. Yu, *Angew. Chem., Int. Ed.*, 2019, **58**, 15772–15777.

39 Y. He, X. Zhu, C. Zhang, Z. Liu, B. Cao, L. Sheng, Y. Yang, Q. Feng, N. Wang, J. Z. Ou and Y. Xu, *ACS Sustainable Chem. Eng.*, 2023, **11**, 5055–5064.
40 P. Zhang, W. Tan, H. He and Z. Fu, *J. Alloys Compd.*, 2021, **853**, 157265–157271.
41 C. Chen, Y. Tuo, Q. Lu, H. Lu, S. Zhang, Y. Zhou, J. Zhang, Z. Liu, Z. Kang, X. Feng and D. Chen, *Appl. Catal., B*, 2021, 287.
42 Z. Chen, K. Huang, B. Zhang, J. Xia, J. Wu, Z. Zhang and Y. Huang, *Int. J. Miner., Metall. Mater.*, 2023, **30**, 1922–1932.
43 P. Li, X. Wan, J. Su, W. Liu, Y. Guo, H. Yin and D. Wang, *ACS Catal.*, 2022, **12**, 11667–11674.
44 S. Wang, D. Yuan, S. Sun, S. Huang, Y. Wu, L. Zhang, S. X. Dou, H. K. Liu, Y. Dou and J. Xu, *Small*, 2024, **20**, e2311770.
45 Q. Wang, J. Li, Y. Li, G. Shao, Z. Jia and B. Shen, *Nano Res.*, 2022, **15**, 8751–8759.
46 A. Loh, X. Li, O. O. Taiwo, F. Tariq, N. P. Brandon, P. Wang, K. Xu and B. Wang, *Int. J. Hydrogen Energy*, 2020, **45**, 24232–24247.
47 J. Ke, J. Zhang, L. Zhang, S. He, C. Zhong, L. Du, H. Song, X. Fang, Z. Zhang and Z. Cui, *ACS Catal.*, 2024, **14**, 16363–16373.
48 G. Huo, X.-W. Wang, Z.-B. Zhang, Z. Song, X.-M. Kang, M.-X. Chen, Q. Wang, X.-Z. Fu and J.-L. Luo, *J. Energy Chem.*, 2020, **51**, 81–89.
49 M. Zhang, X. Zhou, K. Luo, Y. Fan, C. He, Q. Niu, J. Zhang, P. Zhang and S. Dai, *J. Mater. Chem. A*, 2025, **13**, 1287–1301.
50 X. Liu, Y. Xing, K. Xu, H. Zhang, M. Gong, Q. Jia, S. Zhang and W. Lei, *Small*, 2022, **18**, e2200524.
51 F. Zeng, C. Mebrahtu, L. Liao, A. K. Beine and R. Palkovits, *J. Energy Chem.*, 2022, **69**, 301–329.
52 J. E. Park, S. Y. Kang, S.-H. Oh, J. K. Kim, M. S. Lim, C.-Y. Ahn, Y.-H. Cho and Y.-E. Sung, *Electrochim. Acta*, 2019, **295**, 99–106.